

pubs.acs.org/acsaelm Article

# Highly Conductive Nanograting—Nanohole Structures with Tunable and Dual-Band Spectral Transparency

Yanfeng Wang, Inyoung Choi, Kaiyuan Zhang, Yanjun Yang, Shen Ao, Xiaotian Xue, Wangyang Fu, Zhengjun Zhang,\* and Yiping Zhao\*



Cite This: ACS Appl. Electron. Mater. 2021, 3, 3489-3500



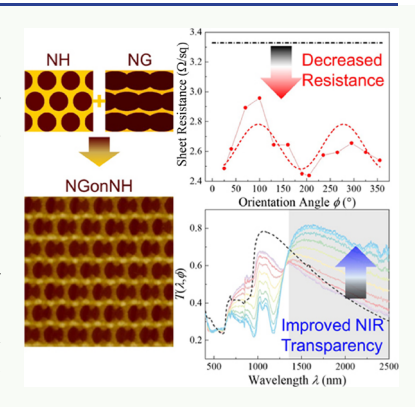
**ACCESS** 

Metrics & More

Article Recommendations

s Supporting Information

**ABSTRACT:** Simultaneously increasing electric conductance and optical transmission represents a key challenge for developing a high-quality transparent metallic film (TMF). Using nanosphere lithography and oblique angle deposition, we show that large-area silver nanograting (NG) on nanohole (NH) structures can meet this challenge. The fabricated NG–NH hybrid structure exhibits an excellent sheet resistance as low as 4.53  $\Omega$ /sq, an optical transmission of 75.4% from visible to near-infrared, and a high Haacke number up to 13.1, which is superior to that of previously reported metal NH networks or TMFs. Both the electric conductance and optical transparency are anisotropic and can be tuned by the NH diameter, lattice spacing, and the polarization of incident light. In particular, the transparency wavelength bands for different polarized lights are significantly different, which can be used for dual functionalities. The anisotropic electronic property is explained by a two-dimensional resistor network model, and the observed optical responses match well with the results from finite-difference time-domain calculations.



**KEYWORDS:** nanograting, nanohole, extraordinary optical transmission, tunable transmission, tunable conductivity, transparent conductive films

## 1. INTRODUCTION

Recently there have been increasing interests in designing innovative transparent metallic films (TMFs) for flexible optoelectronic devices because of their inherently high electrical conductivity, optical transparency, mechanical robustness, and cost-competitiveness. 1,2 TMFs are perforated thin metallic networks with a low filling ratio that allows light to transmit through.<sup>3</sup> So far, metallic nanostructure arrays, including nanowires, <sup>3-5</sup> nanogratings (NGs), <sup>3,6</sup> and nanoholes <sup>10</sup> have been reported as promising TMFs. Metallic nanowire TMFs usually show a relatively low conductivity (sheet resistance >10  $\Omega/\text{sq}$ )<sup>3,5,11,12</sup> due to the high wire-towire junction resistances. The NGs can only be used for onedirectional conduction and transmission.<sup>6</sup> However, the metallic NH array shows high conductance due to the highly connected metal mesh structure<sup>8</sup> and good optical transmission resulting from the extraordinary optical transmission (EOT) effect. <sup>13</sup> Table 1 summarizes the performance of NHbased TMFs reported in the literature. These NHs have been used in various wavelength regions for different applications, including the ultraviolet region for nonlinear optics, 14 the visible region for touchscreen displays, <sup>10,15,16</sup> the near-infrared (NIR) region for medical applications, <sup>17</sup> the terahertz region for imaging, 18 and so on. The fabrication of NHs with adjustable structure parameters can be achieved by nanosphere lithography (NSL).<sup>7,19</sup> It is inexpensive and can achieve waferscale production with a large variety of conducting materials.

Even though the NH TMFs have attracted a lot of attention, they also have two notable shortcomings. First, the NH TMFs have a relatively small transparency spectral window (see Table 1) due to the reflective losses, the finite perforation fraction  $(PF = 1 - A_m/A_0)$ , where  $A_0$  is the total area of the film and  $A_m$ is the metal covered area), and Wood's anomaly (where the light could not be transmitted due to the light diffraction parallel to the structure surface).<sup>20</sup> It has been discovered that the transmittance and spectral width can be improved by increasing the PF or decreasing the film thickness (to be less than 10 nm). 10,21 However, the thickness of the NH film and the width of the NH network determine the conductance of the TMFs. It is well known that thicker films and larger width of the network provide a larger metal cross-sectional area, thus significantly increasing the conductance of the TMFs. However, such a change is contradictory to the requirements for higher transparency, which refers to lower film thickness and smaller network width (i.e., larger PF).

Clearly, to just tune the conventional NH parameters such as hole diameter and period as well as film thickness is not

Received: May 19, 2021 Accepted: July 30, 2021 Published: August 6, 2021





Table 1. Average Transmittance and Sheet Resistance for Several NH Array-Based Transparent Conducting Electrodes

NH array	thickness (nm)	PF	sheet resistance	average transmittance	FOM $\Phi_{\rm H}$	refs
Ag NH array	50	0.65	$6.1 \Omega/\text{sq}$	62.1% (300–1200 nm)	1.4	8
	10	0.7	$35 \Omega/sq$	~85% (425-800 nm)	5.6	10
Au NH array	_	_	$6.2 \Omega/\text{sq}$	65% (300-1200 nm)	2.2	8
	40	0.73	104.5 $\Omega/\text{sq}$	89% (550 nm)	3.0	30
	40	0.62	16.5 $\Omega/\text{sq}$	65% (550 nm)	0.8	
Cu NH array	50	0.42	$3 \Omega/sq$	~50% (400-2000 nm)	0.3	3
	8	0.43	$16.3 \ \Omega/\text{sq}$	56.9% (450-800 nm) 67.4% (1.09 THz)	0.2	18
TiO <sub>2</sub> /Au/TiO <sub>2</sub> NH array	9/12/9	0.58	$70~\Omega/\mathrm{sq}$	~78% (400-900 nm)	1.2	16
Ag NH array	50	0.60	4.52 $\Omega/\text{sq}$	64.9% (1000-2500 nm)	2.9	this work
	50	0.59	$3.62 \Omega/\text{sq}$	51.8% (1000-2500 nm)	0.4	
Ag NGonNH	50	0.55	4.53 $\Omega/\text{sq}$	75.4% (1000–2500 nm)	13.1	
	50	0.55	$3.07 \Omega/\text{sq}$	65.0% (1000–2500 nm)	4.4	

 $<sup>^</sup>a$ The "Haacke" number or FOM  $\Phi_{
m H}$  is calculated based on the average nonpolarized transmittance in the wavelength region shown in the brackets.

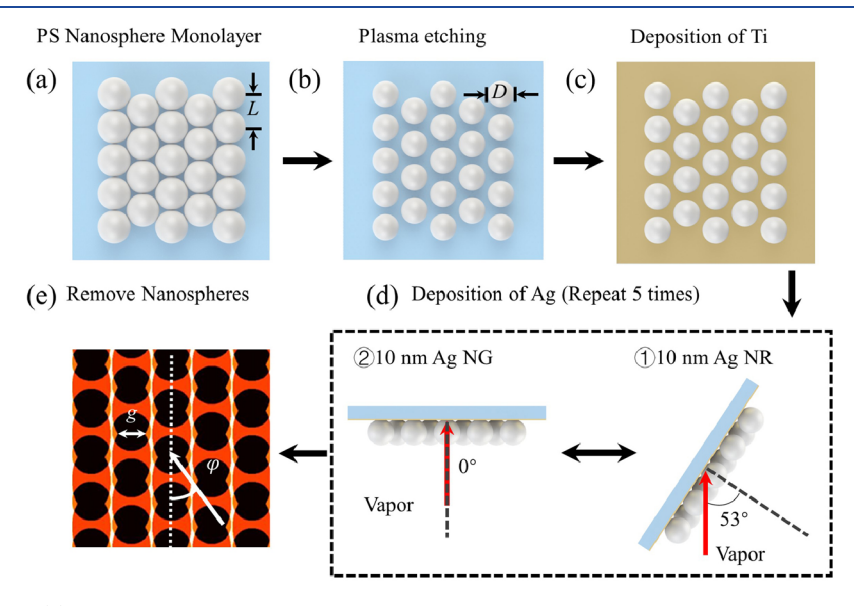


Figure 1. Fabrication scheme: (a) monolayer of PSNS with a diameter of L = 500 or 750 nm was formed on a clean glass slide. (b) Monolayer was  $O_2$  plasma-etched to a smaller diameter D. (c) Ti thin film (3 nm thick) was deposited at  $\theta = 0^{\circ}$  followed by (d): ① 10 nm of Ag NG layer deposition at  $\theta = 53^{\circ}$  and ② 10 nm Ag NH layer deposition at  $\theta = 0^{\circ}$ . Both ① and ② steps were repeated five times to form a 50 nm NGonNH layer. (e) Predicted NGonNH structure by an in-house MATLAB program after removing the PSNS layer by Scotch tape.  $\varphi$  is defined as the angle formed by the projection of the incident vapor (white arrow) on the substrate and an imaginary line that passes through centers of one row of PSNS (white dashed line).

adequate to significantly improve the performance of NH TMFs. Thus, alternative strategies should be investigated. For example, multilayer transparent conductive oxide (TCO) and metal NH (TCO/metal NH/TCO) structures have been investigated to simultaneously improve the optical transparency and electrical properties. However, the fabrication strategy is rather complicated, but the performance is not significantly improved. Recent studies have shown that when NH changes to compound nanostructures, such as nanoparticle in NHs, and an anorods in NHs, the EOT-related property can be tuned significantly due to the plasmonic coupling effect or hybridization. We have hypothesized that if the nanostructure is selected appropriately, the conductance of the compound structure (i.e., NH + another nanostructure) could also be improved along with the tuned optical properties.

In this work, we address the contradiction of transparency and conductivity of metallic nanostructures by overlapping NH with NG. NSL and oblique angle deposition (OAD) were used to fabricate large-area silver NG on NH (NGonNH) structures. The resulting NGonNH structures have shown reduced anisotropic resistances when compared to the pure NH array due to the increased film thickness along the grid orientation. A two-dimensional hexagonal network model was built to understand the anisotropic electrical properties. Highly improved transmission with tunable transmission spectral ranges was also obtained due to the plasmonic coupling effect and can be predicted by finite-difference time-domain (FDTD) calculations. Better transmittance—sheet resistance trade-off can be seen when comparing the "Haacke" figure of merit (FOM) of the NGonNH structure to those of other published NHs or transparent conductive films (TCF). The switchable polarization-dependent transmission regions (visible and NIR) can be used for dual functionalities in different wavelength bands under different application scenarios.

# 2. EXPERIMENTAL SECTION

**2.1. Materials.** Polystyrene nanospheres (PSNS) with diameters of 500 and 750 nm (Polyscience, Lot# 679675 and Lot# 687640) and ethanol (Sigma-Aldrich, 98%) were used to form the nanosphere

monolayers on cleaned glass slides (Gold Seal, Part# 3010). Sulfuric acid (Fisher Scientific, 98%), ammonium hydroxide (Fisher Scientific, 98%), and hydrogen peroxide (Fisher Scientific, 30%) were used to clean the substrates. Silver (Plasmaterials, 99.99%) and titanium pellets (Kurt J. Lesker, 99.995%) were purchased as the evaporation materials. Deionized (DI) water (18  $\mathrm{M}\Omega$  cm) was used throughout the experiments. All chemicals and materials were used without further purification.

2.2. Fabrication of Ag NGonNH. The fabrication process of NGonNH utilizing the NSL and shadowing growth technique is schematically illustrated in Figure 1.<sup>28,31-33</sup> A hexagonally closepacked monolayer of PSNS with an initial diameter of L = 500 or 750 nm was prepared on glass substrates by an air-water interface method (Figure 1a). The procedure was described in detail in several previous publications. 34-36 The size of the PSNS on the substrates was shrunk to a smaller diameter D via a reactive ion etching (RIE, Trion Phantom III RIE/ICP) with varied etching times, as shown in Figure 1b. The etched PSNS monolayer-coated substrates were loaded into a custom-built electron-beam deposition system and mounted on a substrate holder with one motor to control the polar rotation angle  $\theta$ (the angle between the substrate surface normal and the vapor deposition direction). The vacuum chamber was pumped down under a base pressure of  $<10^{-6}$  Torr, and the monolayer-coated substrates were positioned to face normally in the vapor deposition direction. All the deposition thickness and rates were monitored by a quartz crystal microbalance facing the source. Then, a 3 nm thick Ti was deposited to promote the adhesion of the subsequent Ag layer (Figure 1c). Ag nanostructures of different morphologies were prepared with the deposition configuration shown in Figure 1d. First, the NG structure (the white stripelike patterns in Figure 1e) was formed in the vacancies between the PS particles when the deposition angle was set as  $\theta = 53^{\circ}$ . To make sure that the vapor would pass through the gap between two adjacent PSNS to form an NG structure on the substrate, the monocrystalline monolayers with an area of about 1 cm<sup>2</sup> was aligned in the direction of  $\varphi = 0^{\circ}$  ( $\varphi$  is defined as the angle formed by the projection line (white arrow in Figure 1e) of the incident vapor and an imaginary line (white dashed line in Figure 1e) that passes through centers of one row of PSNS by a laser diffraction apparatus.<sup>37</sup> It should be noted that the uniformity and orientation of the PSNS masks are crucial for the fabrication of these complex nanostructures and are verified through the laser diffraction patterns. A 10 nm thick Ag was deposited at a deposition rate of 0.05 nm/s to form the NG structure. Then, another 10 nm thick Ag was deposited at  $\theta = 0^{\circ}$  to form the NH structure. These two steps were repeated five times to achieve the final NGonNH structures. Such a deposition strategy was chosen to minimize the shadowing effect due to the increased film thickness at NG deposition 35,38 and to establish the connectivity of NG on NH (see Section S1 for details). After the Ag deposition, the PSNS monolayer was removed using Scotch tape and the substrates were rinsed in toluene, acetone, and 2-propanol successively to remove the PS residues.

2.3. Morphological, Optical, and Electrical Characterizations. The morphology of the resulting NGonNH structures was characterized by atomic force microscopy (AFM, Park Systems NX-10 AFM) and field-emission scanning electron microscopy (SEM, Zeiss GeminiSEM 500). Both the SEM and AFM images were analyzed by the ImageJ software (NIH). The orientation-angle-dependent sheet resistance measurements were performed by depositing 200 nm thick Ag electrode patterns via a specially designed shadow mask (see Section S2) and measured by a four-point probe method using a homemade probe station equipped with the FS-Pro semiconductor analyzer. The spring-loaded electric probes were pressed against the electrodes under the observation of an optical microscope. The optical transmission spectra of the structures were measured by an ultraviolet-visible spectrophotometer (UV-vis, Jasco-750), and a 40× objective lens was added between the incident light and sample surface to focus the incident light to a smaller area. Polarization angledependent spectra were achieved by adding a matched set of polarizers to the Jasco system via a home-built mounting and alignment system (see Section S3).

**2.4. Numerical Calculations.** An in-house MATLAB program was used to predict the Ag pattern on the substrate based on the deposition configuration in Figure 1d.  $^{35,36}$  This calculation predicted the pattern and thickness distribution of the Ag film on the substrate by considering the shadowing effects from 36 nearest-neighbor PSNS. An example of the calculated NGonNH structure with L=500 nm and D=340 nm is shown in Figure 1e. The definitions of D, L, and the gap distance g between the NG are also shown in Figure 1.

A commercial software package (Ansys Lumerical 2020 R2 Finite Difference IDE) was used to calculate the polarization angledependent transmission spectra and electric field (E-field) distributions of the Ag NGonNH structures. The MATLAB calculated results were imported into the FDTD software as the calculation models. The thicknesses of NH  $(h_{\rm H})$  and NG  $(h_{\rm G})$  were set to be 50 and 45 nm, respectively, based on the experimental results (the definitions of  $h_{\rm H}$  and  $h_{\rm G}$  are shown in Figure S4). A unit cell (see Section S4) was set as the calculation area with periodic boundary conditions in the two lateral dimensions. Perfectly matched layer boundary conditions were used on the top and bottom surfaces of the calculation domain. Monitors of "frequency-domain field and power" and "frequencydomain field profile" were set up to determine the transmission spectra and localized E-field distribution, respectively. The optical parameters for Ag and the glass (SiO<sub>2</sub>) substrate were taken from Palik's handbook.

# 3. RESULTS AND DISCUSSION

**3.1. Structural Morphology.** Figure 2a-d shows some representative AFM images of the NGonNHs for L = 750 nm

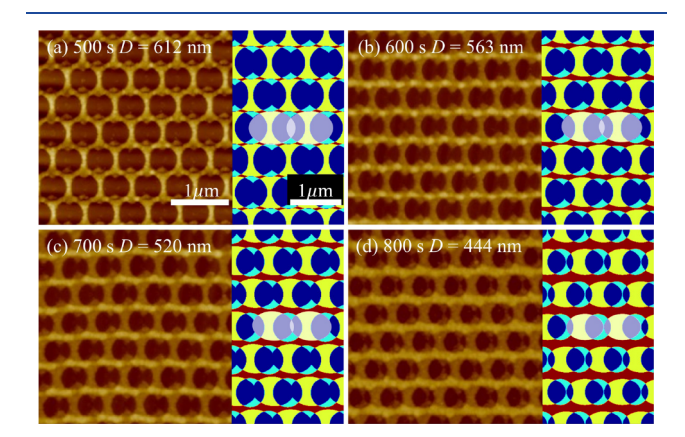


**Figure 2.** Representative AFM images and corresponding MATLAB predicted patterns of the NGonNHs for L=750 nm with a different PSNS etching time t or diameter D. (a) t=500 s, D=612 nm; (b) t=600 s, D=563 nm; (c) t=700 s, D=520 nm; and (d) t=800 s, D=444 nm. The white shaded areas in the predicted images show the elliptical shadows of two adjacent PSNS at  $\theta=53^\circ$  and  $\varphi=0^\circ$ , and the projected vapor incident direction is from right to left.

monolayers but etched at a different t. The AFM images of the pure NH array under the same conditions are shown in Figure S6. The immediate right to each AFM image is the corresponding MATLAB calculated pattern. The NGonNH structure has two layers: the bottom layer is an interconnected NH structure that guarantees the conductivity of the entire TMF, while the NG structure deposited by OAD is on top of the NH structure. The spacing between the centers of adjacent NHs or adjacent grids of the NG was L=750 nm. In the calculated patterns, the white shaded areas are the projected elliptical shadows generated by the two adjacent nanospheres at  $\theta=53^{\circ}$ . The NG could only grow into the brown and cyan areas that are not shaded. Clearly, due to the partial overlap of the elliptical shadows of the nanospheres in the simulated

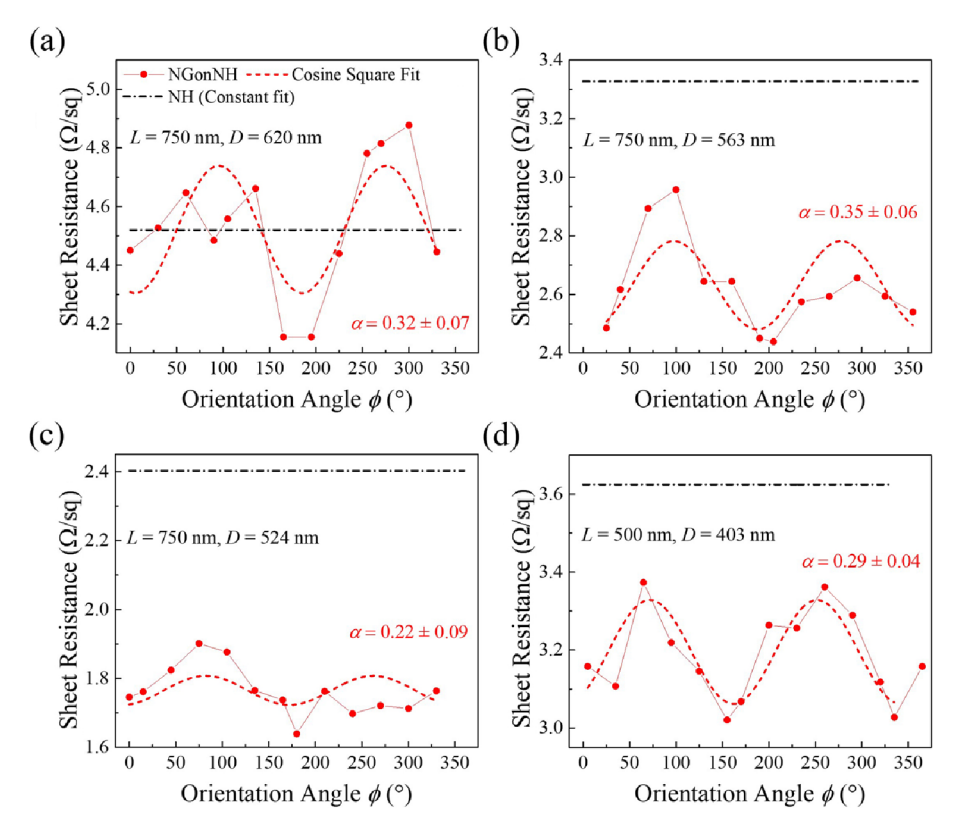


**Figure 3.** Orientation-angle-dependent resistance measurement results of some representative NGonNHs: (a) L = 750 nm, D = 620 nm; (b) L = 750 nm, D = 563 nm; (c) L = 750 nm, D = 524 nm; and (d) L = 500 nm, D = 403 nm. The straight dash-dotted lines represent the average sheet resistance  $R_{\rm NH}$  of the corresponding pure NH arrays, and red dashed curves are squared cosine fitting results for the NGonNH structures.

patterns, the two sides of the grating became serrated, which caused two triangle-like shapes (cyan) formed inside the NH as evidenced in corresponding AFM images. With the decrease in D, the overlap area between the neighboring projected shadows decreases, the nonshaded area becomes larger, and the NG becomes wider. The two triangles also grow larger and the distance g between them decreases. Figure S7a plots g versus D extracted from AFM images. The g decreases from 424 to 200 nm when D changes from 621 to 520 nm. As D further decreases, the projected shadows gradually become tangent to each other, and when D reaches 444 nm (Figure 2d), there are gaps formed between adjacent elliptical shadows; thus, the NGs connect to each other through the connected triangles. In fact, under this condition, it is expected that an elliptical NH array would be formed on top of the NH arrays, so the entire structure is an overlap of two NH arrays: the bottom one is the circular NH array, and the top is elliptical NH array with smaller dimension. From the AFM analysis, the thicknesses of the NGs and NHs for all structures remain almost unchanged,  $h_G \approx 43 \pm 3$  nm for NGs and  $h_H \approx 52 \pm 1$ nm for NHs (Figure S7b).

In addition to D,  $\varphi$  is another important factor that could strongly influence the final patterns. Figure S8 shows some experimental structures and calculated patterns for  $D\approx 612$  nm and L=750 nm but with different  $\varphi$ . As  $\varphi$  changed from 0° to 30°, the NG inside each hole gradually tilted and disconnected with each other, and finally, nanorods in NH structures were formed at  $\varphi=30^{\circ}.^{28}$  Therefore, to form uniform large-area NGonNH structures, two key factors are important: a large-area single-domain PSNS monolayer, and

the azimuthal alignment of the domain orientation to the vapor deposition direction.

3.2. Orientation Angle-Dependent Sheet Resistance. As the geometry of the NGonNH structures are anisotropic, as shown in Figure 2, the sheet resistance R is also orientation dependent. This is why a special electrode shadowing mask was designed (Section S2), so that the orientation-angle  $\phi$ dependent  $R_{\mathrm{GH}}(\phi)$  of the NGonNH structure can be measured. Here, the orientation angle  $\phi$  is defined as the angle between the four-probe alignment direction and the grid orientation of the NGs, which is similar to  $\varphi$  defined in Figure 1e. Both  $R_{\rm GH}(\phi)$  of the selected NGonNH structures and the average sheet resistance  $R_{\rm NH}$  of the corresponding pure NH arrays are plotted in Figure 3. Regardless of the L and D, the  $R_{\rm GH}(\phi) \sim \phi$  relationship follows a similar trend, i.e.,  $R_{\rm GH}(90^\circ)$  $> R_{\rm GH}(0^{\circ})$ , though there were different fluctuations in the measurements. While for NH, the  $R_{\rm NH}$  is independent on  $\phi$ . In fact, for the NGonNH structure, the  $R_{\rm GH}(\phi)$  follows:

$$R_{\rm GH}(\phi) = R_{\rm G}(1 - \alpha^2 \cos^2 \phi) \tag{1}$$

where  $\alpha^2$  represents the conductivity anisotropy of the structure. Note that the larger the  $\alpha$ , the stronger the  $\phi$  dependence. The red dashed curves in Figure 3 are the fitting results based on eq 1. Compared to Figure 3a—c,  $\alpha$  decreased slightly from 0.32 to 0.22 when D decreased from 620 to 524 nm for L=750 nm. For L=500 nm, when D decreased from 426 to 403 nm,  $\alpha$  decreased from 0.33 to 0.29 (see Figure S9). According to statistic t-test, the change in the  $\alpha$  values for different D and L is insignificant within the 95% confidence interval. In addition, the overall resistance of NGonNH decreases with D, and the angle-averaged resistance  $R_{\rm GH}$  for

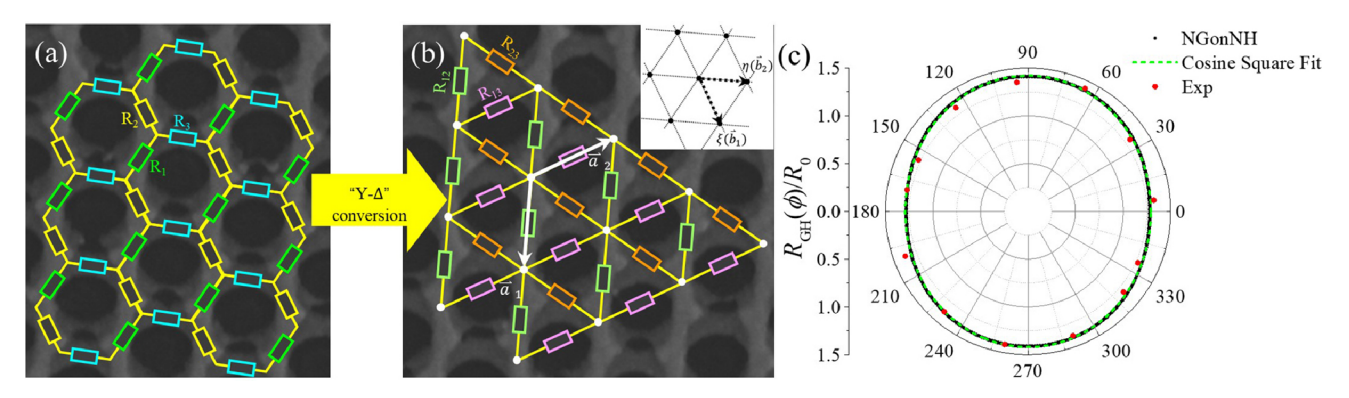


Figure 4. (a) Schematic of the infinite two-dimensional hexagonal lattice of unidentical resistors  $R_1$ ,  $R_2$ , and  $R_3$ . (b) Schematic of the two-dimensional triangular lattice of unidentical resistors  $R_{12}$ ,  $R_{23}$ , and  $R_{13}$  transformed from the hexagonal lattice in (a).  $\vec{a_1}$  and  $\vec{a_2}$  are unit vectors of the unit cell in the lattice with a lattice constant  $L = |\vec{a_1}| = |\vec{a_2}|$ . The inset figure shows the reciprocal lattice that is the Fourier transform of the lattice

in (b) and is generated by reciprocal lattice vectors  $\vec{b_1}$  and  $\vec{b_2}$ . Note that  $[\vec{a_1} \ \vec{a_2}] \begin{bmatrix} \vec{b_1} \\ \vec{b_2} \end{bmatrix} = \begin{bmatrix} 1 \\ 1 \end{bmatrix}$ . (c) Polar plot of the calculated resistance ratio

 $R_{\rm GH}(\phi)/R_0$  for N=50 ( $R_1=R_2=0.25R_0< R_3=R_0$ ) based on eq 4. Red dots are the normalized experimental resistance from Figure 3d. Green dashed curve is the fitting result based on eq 1.

the NGonNH structures decreased from 4.53 to 2.62 and 1.76  $\Omega$ /sq when D decreased from 620 to 563 and 524 nm for L = 750 nm. For L = 500 nm, when D decreased from 426 to 403 nm,  $R_{\rm GH}$  decreased from 5.05 to 3.07  $\Omega/{\rm sq}$ , as shown in Figure S10. The decrease in  $R_{GH}$  with D can be intuitively understood as the overall void area in the film decreases when D decreases (see Figure 2). On comparing  $R_{\rm GH}(\phi)$  with the corresponding sheet resistance  $R_{NH}$  of pure NH (the black dashed line), except for Figure 3a,  $R_{\mathrm{GH}}(\phi)$  is always smaller than the corresponding  $R_{\mathrm{NH}}$ , which indicates a great improvement in conductance for the NH and NG combined NGonNH structures. Even in Figure 3a,  $R_{\rm GH}(0^\circ)$  is smaller than the corresponding  $R_{\rm NH}$ , and the angle-averaged resistance  $R_{\rm GH}$ (4.53  $\Omega/\text{sq}$ ) is comparable to the corresponding  $R_{\text{NH}}$  (4.52  $\Omega/$ sq). The conductance in Figure 3 is comparable to or surpass the best values reported in metal NH arrays, as shown in Table 1,3,8,10 and is higher than those of traditional TCOs,40-44 the state-of-the-art carbon nanotubes, <sup>45</sup> graphene films, <sup>46</sup> and metal nanowire networks <sup>3-5,9,11,12</sup> (Table S1). The improvement in the conductivity performance of the NGonNH structures can be intuitively understood as the resistance decreases with the increased volume of the conductive material or the effective thickness. In fact, such an improved and  $\phi$ dependent resistance can be understood by a resistor network model.

Based on the geometry and the periodicity of the structure, as shown in Figure 4a, a network resistor model is proposed. The NGonNH structures can be viewed as an infinite honeycomb lattice of unidentical unit resistors  $R_1$ ,  $R_2$ , and  $R_3$ , as shown in Figure 4a, and unit resistors  $R_i$  (i = 1, 2, 3) can be estimated as

$$R_i = \rho \cdot k_i \frac{l_i}{w_i t_i} \tag{2}$$

where  $t_i$  and  $w_i$  are the effective thickness and width of unit metal arm, and  $k_i$  is a modification coefficient to the resistivity when the thickness or the width of individual metal arm is comparable to the mean free path of the metal,<sup>47</sup> or there is a significant grain boundary effect.<sup>47,48</sup> For the NH structure,  $R_1 = R_2 = R_3$ , while for the NGonNH structures, unit resistors

along different directions are of different values due to different Ag film thicknesses (different  $t_i$ ) and the overlapped Ag materials/shape (different  $w_i$ ). A "Y $-\Delta$ " conversion is performed to obtain a triangular lattice of identical lattice points with resistors  $R_{12}$ ,  $R_{23}$ , and  $R_{13}$ , as shown Figure 4b, 49 where

$$\begin{split} R_{12} &= \frac{R_1 R_2 + R_2 R_3 + R_1 R_3}{R_3}, \, R_{13} = \frac{R_1 R_2 + R_2 R_3 + R_1 R_3}{R_2}, \\ R_{23} &= \frac{R_1 R_2 + R_2 R_3 + R_1 R_3}{R_1} \end{split} \tag{3}$$

The equivalent resistance between a fixed lattice point (0, 0) and an arbitrary lattice point (m, k) can be calculated as

$$R_{00-mk} = \frac{1}{4\pi^2} \int_{-\pi}^{\pi} \int_{-\pi}^{\pi} \times \frac{R_{12}R_{23}R_{13}(1 - \cos(m\xi + k\eta))}{R_{12}R_{23}(1 - \cos\eta) + R_{23}R_{13}(1 - \cos\xi) + R_{12}R_{13}(1 - \cos(\xi + \eta))} \times d\xi d\eta$$
(4)

The detailed derivation can be found in Section S8. Take  $\vec{a_1}$ ,  $\vec{a_2}$  as unit vectors in the hexagonal lattice with a lattice constant  $L = |\vec{a_1}| = |\vec{a_2}|$ , then, the arbitrary lattice location (m, k) is expressed as  $\vec{r} = m\vec{a_1} + k\vec{a_2}$ , where m and k range through all integer values. The lattice position (m, k) on a circle with a fixed radius N from the fixed origin point (0, 0) should satisfy  $m^2 + k^2 - mk = N^2$ , and the corresponding  $\phi$  angle can be calculated based on

$$\cos \phi = \frac{m - \frac{k}{2}}{\left(m - \frac{k}{2}\right)^2 + \frac{3}{4}k^2} \tag{5}$$

Thus, based on eqs 4 and 5, the  $\phi$ -dependence network resistance can be estimated.

For a pure NH structure,  $R_1 = R_2 = R_3 = R_0 = \rho \cdot k_0 (l_0/w_0 t_0)$ ; for a fixed D and L, 4 changes to

$$\frac{R_{00-mk}^{\rm NH}}{R_0} = \frac{3}{4\pi^2} \int_{-\pi}^{\pi} \int_{-\pi}^{\pi} \frac{1 - \cos(m\xi + k\eta)}{3 - \cos\xi - \cos\eta - \cos(\xi + \eta)} d\xi d\eta$$

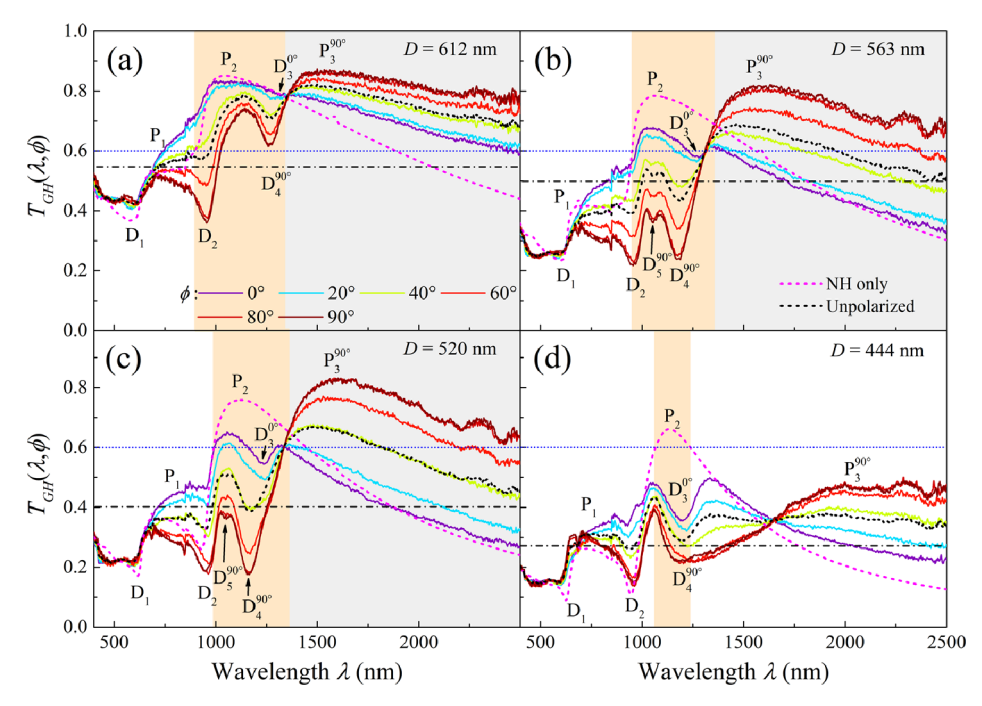


Figure 5. Polarization angle-dependent transmission spectra (solid curves)  $T_{\rm GH}(\lambda,\phi)$  of the NGonNH structures shown in Figure 2. (a) L=750 nm, D=621 nm; (b) L=750 nm, D=563 nm; (c) L=750 nm, D=520 nm; and (d) L=750 nm, D=444 nm. Nonpolarized  $T_{\rm GHO}(\lambda)$  of the NGonNH structures (black dashed curve) and the corresponding NH array (magenta dashed curve) are plotted as references. The black dashedotted lines in the figure show the PF of each sample, the blue dotted lines in the figure show T=0.6, and the orange shaded area represents the wavelength region where  $T_{\rm NH}(\lambda)>0.6$  and  $T_{\rm NH}(\lambda)>T_{\rm GH}(\lambda,90^\circ)$ , the gray shaded area is the wavelength region where  $T_{\rm CH}(\lambda,90^\circ)>0.6$  and  $T_{\rm CH}(\lambda,90^\circ)>T_{\rm NH}(\lambda)$ .

For N = 50, the integration gives  $R_{\rm NH}/R_0 \sim 3.16$ , as shown in Figure S12. For the NGonNH structures, after the combination of pure NH and NG structures, based on the AFM images in Figure 2, the thicknesses  $t_1$  and  $t_2$  as well as the widths  $w_1$  and  $w_2$  of the resistors  $R_1$  and  $R_2$  have roughly doubled compared to  $t_0$  and  $w_0$ . Assuming that  $R_3 = R_0$  and  $R_1 = R_2 = c \cdot R_0$ , where c is estimated to be 0.25, then eq 4 can be rewritten as

$$\frac{R_{00-mk}^{\rm GH}}{R_0} = \frac{1}{4\pi^2} \int_{-\pi}^{\pi} \int_{-\pi}^{\pi} \frac{c(c+2)(1-\cos(m\xi+k\eta))}{c(1-\cos\eta)+1-\cos\xi+c(1-\cos(\xi+\eta))}$$

$$\frac{d\xi d\eta}{dt} dt$$

The calculated  $R_{\rm GH}(\phi)/R_0$  for N=50 is shown in Figure 4c. Two characteristics are exhibited: first, for any  $\phi$  angle,  $R_{\rm GH}(\phi)/R_0$  (<1.5) is always smaller than  $R_{\rm NH}/R_0$ ; second, the polar plot of  $R_{\rm GH}(\phi)/R_0$  shows maxima at  $\phi=90^\circ$  and 270° and minima at  $\phi=0^\circ$  and 180°, which demonstrates the strong  $\phi$  dependence. For comparison, the polar plot of the normalized resistance of one of the representative experimental results (Figure 3d) is also shown in Figure 4c, which also shows maximums at  $\phi=90^\circ$  and 270°. Similar to the experimental results, the calculated  $R_{\rm GH}(\phi)$  can be well fitted by the cosine-square function (the green dashed curve). Clearly, the network model predicts well the experimental results.

**3.3. Spectral Tunable Transmission at NIR.** In addition to excellent electrical properties, good optical transmissions in a large wavelength region are also required for TMFs. The photos of one of the NGonNH samples (L=750 nm, D=612 nm) taken from different angles are shown in Figure S13, showing visible transparency. The representative polarization angle-dependent transmission spectra  $T_{\rm GH}(\lambda, \phi)$  of the NGonNH structures are presented in Figure 5. Here, the

light incident angle is  $0^{\circ}$  and the polarization angle  $\phi$  is defined as the angle between the polarization direction of the incident light and the grid orientation of the NGs, which is consistent with the  $\phi$  angle for resistance measurements. In general,  $T_{\rm GH}(\lambda, \phi)$  changes with  $\phi$  and shows polarization switchable high transmission bands at visible ( $\phi = 0^{\circ}$ ) and NIR regions  $(\phi = 90^{\circ})$ . The extinction ratios for different NGonNH structures (ER =  $10 \log(T_{GH}(\lambda, 90^{\circ})/T_{GH}(\lambda, 0^{\circ}))$ ) are shown in Figure S14. The black dash-dotted lines in the figure show the PF of each sample, and the transmission/PF ratios are larger than 1 in most wavelength regions, which is orders of magnitude greater than that predicted by the standard aperture theory  $(T \sim (D/2\lambda)^4)$ , demonstrating obvious EOT phenomenon. To understand the  $T_{\rm GH}(\lambda, \phi)$  spectra, unpolarized  $T_{\rm GH0}(\lambda)$  of the NGonNH structures (black dashed curve) and  $T_{NH}(\lambda)$  of the pure NH arrays with the same D and L (magenta dashed curve) are also plotted in the corresponding figures. Regardless of the D, the  $T_{\rm NH}(\lambda)$  spectra possess two EOT peaks (P1 and P2) caused by the surface plasma resonance at the Ag-air and Ag-glass interfaces and two Wood's anomaly dips  $(D_1 \text{ and } D_2)^{20}$  Compared to  $T_{\rm NH}(\lambda)$ , the  $T_{\rm GH}(\lambda, \phi)$  spectra show richer spectral features. The most notable difference is the highly improved transmission at the NIR region and the strong  $\phi$ -dependent optical responses due to the breaking of structural symmetry. The trend of  $T_{\rm GH}(\lambda, \phi)$  for different *D* is very similar: when  $\phi = 0^{\circ}$ ,  $T_{\rm GH}(\lambda, 0^{\circ})$  is similar to  $T_{\rm NH}(\lambda)$  but with a dip,  $D_3^{0^{\circ}}$ , on top of the peak  $P_2$ . The transmission intensity T around  $P_2$  is suppressed because of the appearance of  $D_3^{0^{\circ}}$ . When  $\phi$  changes from  $0^{\circ}$  to  $90^{\circ}$ , another dip  $D_4$  appears near  $D_3^{0^{\circ}}$  and a new peak P<sub>3</sub> also emerges in the infrared wavelength region.  $T_{\rm GH}(\lambda,$  $\phi$ ) around  $\lambda_{
m D_2}$  and  $\lambda_{
m D_4}$  gradually decreases with  $\phi$ , while

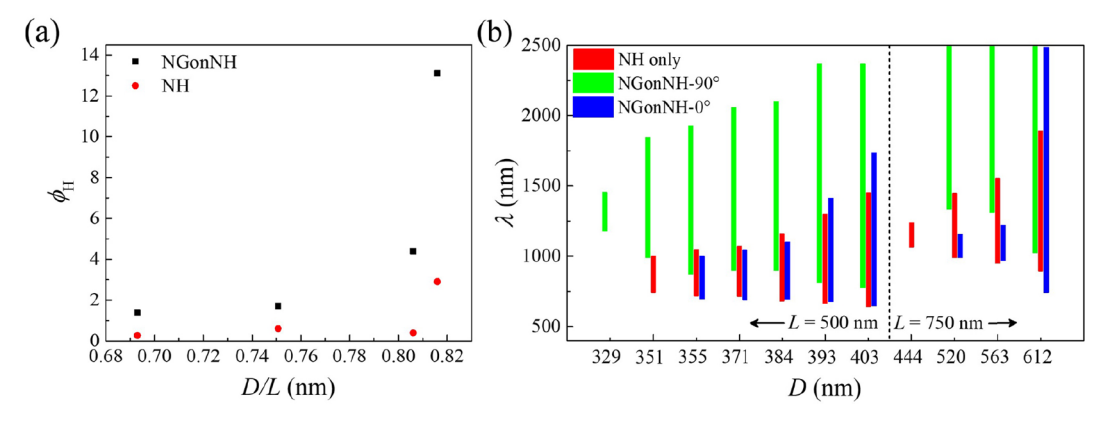


Figure 6. (a) Calculated Haacke number  $\Phi_{\rm H}$  for the NGonNH structures and the corresponding NH with the same D/L ratio. The transmission T used to calculate  $\Phi_{\rm H}$  are based on the averaged nonpolarized transmittance from 1000 to 2500 nm. (b) Comparison of the wavelength region with transmittance larger than 0.6 for  $T_{\rm NH}(\lambda)$  for the NH structures, and  $T_{\rm GH}(\lambda, 90^\circ)$  and  $T_{\rm GH}(\lambda, 0^\circ)$  for the NGonNH structures for L=750 and 500 nm; the left side of the black dashed line is for L=500 nm, while the right side is for L=750 nm.

 $T_{\rm GH}(\lambda, \phi)$  around  $\lambda_{\rm P}$  gradually increases with  $\phi$ . When  $\phi$ 90°, the peak  $P_3^{90°}$  dominates, and  $T_{GH}(\lambda, 90°)$  around and after  $\lambda_{p_2^{90^{\circ}}}$  is highly improved when compared to that of  $T_{\rm NH}(\lambda)$ , even though the PF of the whole structure decreases. For example, compared to  $T_{\rm NH}(\lambda)$ ,  $T_{\rm GH}(\lambda, 90^{\circ})$  is nearly doubled over a wide spectral region (i.e., from 1500 to 2500 nm) after the NG was added on NH, as shown in Figure 5c. As we know that the skin depth  $\delta$  of metal such as silver is in the range of 10–20 nm at  $\lambda$  = 550 nm. As  $\lambda$  increases,  $\delta$  also increases, which causes a dramatic increase in the reflection. Therefore, thin metal or metal nanostructure films have poor NIR transmittance. 45 However, the NGonNH structures show highly improved NIR transmittance, i.e., the average nonpolarized  $T_{\rm GH0}(\lambda)$  between  $\lambda = 1500$  and 2500 nm increased by ~19% compared to  $T_{\rm NH}(\lambda)$ , as shown in Figure S15 and Table S2. The NIR transmittance is very important for infrared

The spectral features in  $T_{\rm GH}(\lambda, \phi)$  can also be tuned by D. When D decreases from 612 to 444 nm, the  $P_3^{90^{\circ}}$  peak can be red-shifted from 1452 to 1998 nm and become very broad. However, the integral transmission at  $P_3^{90^{\circ}}$  decreases. If the transparency threshold is set to be  $T \ge 0.6$  (the blue dotted lines in Figure 5; the value 0.6 is chosen based on the references on the research of NHs shown in Table 1), for the NGonNH with D = 612 nm, the range of wavelengths for  $T \ge$ 0.6 covers almost the entire NIR wavelength region. With the decrease in D, the starting wavelength for the transparency redshifts and the overall wavelength region for transparency becomes narrower. When D = 444 nm, the structures become opaque. The other significant change in  $T_{\rm GH}(\lambda, \phi)$  is the appearance of the small dip  $D_5^{90^\circ}$  at the shorter wavelength side of  $D_4^{90^\circ}$  (D = 563 and 520 nm in Figure 5c,d). In addition, when  $\phi = 0^{\circ}$ , with the decrease in D, the  $D_3^{0^{\circ}}$  dip blue-shifted a little and became deeper with the decreased integral transmission. Figure S16a-c directly compares the  $T_{\rm GH}(\lambda, 0^{\circ})$ ,  $T_{\rm GH}(\lambda, 90^{\circ})$ , and nonpolarized  $T_{\rm GH}(\lambda)$  for different D, and the corresponding  $\lambda_{D_3^{0^\circ}}$ ,  $\lambda_{D_4^{90^\circ}}$  and  $\lambda_{P_3^{90^\circ}}$  are plotted against D in Figure S16d.

As the transmittance around and after  $\lambda_{P_3^{90^\circ}}$  of the NGonNH structure can be greatly enhanced, a wider transmittance-enhanced spectral region can be achieved if  $\lambda_{P_3^{90^\circ}}$  can be tuned

to blue-shift. To this end, a smaller L of the NGonNH structure has been investigated. The AFM images and  $T_{\rm GH}(\lambda,\phi)$  of L=500 nm with different D are shown in Figures S17 and S18. The  $\lambda_{\rm P_3^{90^\circ}}$  shifted from 1570 nm of L=750 nm to 1090 nm of L=500 nm for the NGonNH structure with the D/L ratio  $\sim 0.75$  (Figure S18c), and the transmittance-enhanced spectral region was also expanded from  $\sim 1300-2500$  to  $\sim 1000-2500$  nm. This NIR spectral window, known as the "optical window" or "therapeutic window," is the range of wavelengths that has the maximum depth of penetration in tissue and is very important in many medical applications. To Detailed discussion about NGonNH structures with L=500 nm can be found in Section S11.

3.4. Tunability of the Improved Transmission Waveband. The quality of the TMFs is determined by not only the resistance but also the optical transmission. According to Haacke, 51 the performance of a TMF should be described by the FOM,  $\Phi_{\rm H} = T^{10}/R$ , where R is the sheet resistance and T is the optical transmission of the TMF. Figure 6a plots the  $\Phi_{
m H}$ for the NGonNHs with different D/L ratio together with the corresponding NHs as a reference. The transmission T used to calculate  $\Phi_H$  is based on the averaged nonpolarized transmission from 1000 to 2500 nm. With an increase in the D/Lratio,  $\Phi_{\rm H}$  increases for both the NGonNH and NH structures while  $\Phi_H$  for the NGonNH always remains higher than that of the NH, indicating the improved TMF performance. In particular, for the NGonNH structure with  $D \approx 612$  nm and L= 750 nm,  $\phi_{\rm H}$  = 13.1 ( $R_{\rm GH}$  = 4.53  $\Omega/{\rm sq}$  as shown in Figure 3a and the averaged nonpolarized T from  $\lambda \sim 1000-2500$  nm > 75% as shown in Figure 5a). As shown in Table 1, this value is significantly higher than those reported in other metal NH arrays<sup>3,8,10'</sup> and is comparable to or higher than many previously reported values of TCFs, including TCOs, 40-44 carbon nanotube networks, 45 graphene films, 4 <sup>5</sup> and metal nanowire networks<sup>3-5,9,11,12</sup> (see Table S1). Other NGonNH structures also have a high  $\Phi_{H}$  compared to most TMFs and TCFs reported in Tables 1 and S1. If linearly polarized light is used, the  $\phi_{\rm H}$  of the NGonNH structures under polarized light can be higher than that under nonpolarized light, i.e., the averaged  $T_{\rm GH}(\lambda$ , 90°) for the NGonNH structure with  $D \approx$ 612 and L = 750 nm from  $\lambda \sim 1000-2500$  nm > 78.8%; thus,  $\phi_{\rm H-90^{\circ}} = 20.4 \ (>\phi_{\rm H} = 13.1).$ 

Another important factor for TMFs is the bandwidth of the transparency wavelength region. Clearly, due to the polar-

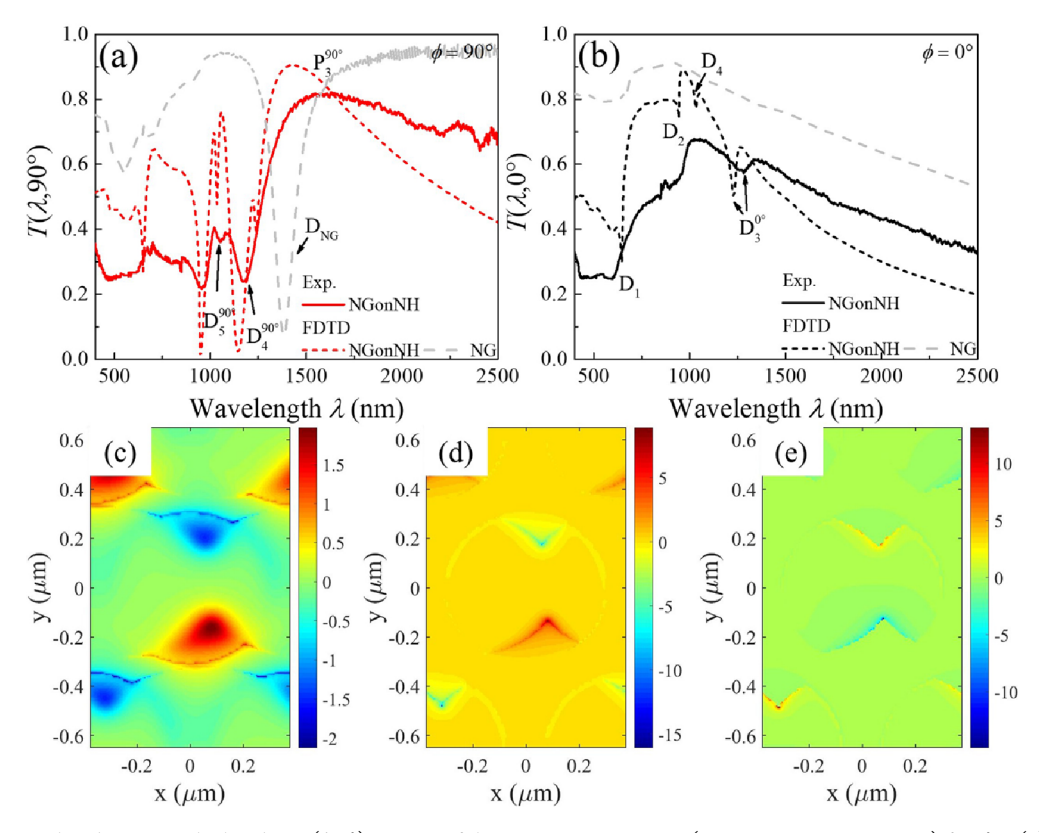


Figure 7. Experimental and FDTD calculated  $T_{\rm GH}(\lambda,\phi)$  spectra of the NGonNH structure (L=750 nm, D=563 nm) for  $\phi=(a)~90^\circ$  and (b)  $0^\circ$ . The gray dashed curves are FDTD calculated  $T_{\rm NG}(\lambda,\phi)$  of the corresponding MATLAB generated NG structure at different  $\phi$ . (c-e)  $E_z$ -field distributions at  $\lambda_{P_3^{30^\circ}}$  at the (c) air-grating interface, (d) grating-hole interface, and (e) hole-glass interface.

ization dependent optical transmission, the resulted NGonNH structures could have switchable optical transparency in different wavelength regions at  $\phi = 0^{\circ}$  and  $90^{\circ}$ . Based on the transparency criteria T = 0.6, the transparency wavelength regions for different L and D as well as polarization angle are extracted and plotted in Figure 6b. For the pure NH structure, the transparency wavelength region  $\Delta \lambda$  is mainly concentrated at the EOT peak P<sub>2</sub>, of which the width is determined by D and the resonance wavelength is governed by L. With the increase in D, the EOT peak P2 becomes wider with higher peak transmission, as shown in Figures S6 and 6b (the red colored bars). The  $\Delta \lambda$  of P<sub>2</sub> can be tuned to blue-shift when L decreases from 750 to 500 nm, which is well characterized in the EOT community.<sup>20</sup> Similarly, with the increase in D, a wider  $\Delta \lambda$  is covered by  $T_{\rm GH}(\lambda, 0^{\circ})$  (the blue colored bars in Figure 6b) and  $T_{\rm GH}(\lambda, 90^{\circ})$  (the green colored bars in Figure 6b) for the NGonNH structures. This wavelength region can also be tuned to blue-shift (red-shift) by L. When L decreased from 750 to 500 nm, the central wavelength region of  $\Delta\lambda$  of  $T_{\rm GH}(\lambda, 90^{\circ})$  blue-shifted from ~1900 to ~1500 nm while that of  $T_{\rm GH}(\lambda, 0^{\circ})$  blue-shifted from ~1100 to 900 nm. A smaller L will allow for high transmittance in the visible region. Moreover,  $T_{GH}(\lambda, 90^{\circ})$  covers almost the whole NIR (800– 2500 nm) as shown in Figure 6b and possess a wider  $\Delta\lambda$  than that of the corresponding  $T_{\rm NH}(\lambda)$ . While  $\Delta\lambda$  of  $T_{\rm GH}(\lambda, 0^{\circ})$ covers a similar wavelength region as that of the corresponding pure NH. In particular, for the NGonNH structures with smaller D (see L = 750 nm, D = 563 and 520 nm; L = 500 nm, D = 371, 355, and 351 nm), the overlap of the  $\Delta \lambda$  from both the  $T_{\rm GH}(\lambda, 0^{\circ})$  and  $T_{\rm GH}(\lambda, 90^{\circ})$  is insignificant, which indicates that these structures are excellent candidates for

switchable TMFs, i.e., the NGonNH structures allow the switchability of different transparent bands simply by switching the polarization angle of the incident light. Such a property is good for applications that need switchable optical transparency at different wavelength regions. For the TMFs, a different transparency window is required for different applications, i.e., the visible region for photoelectric devices and electronic products such as flat-panel displays, NIR for medical applications such as optical imaging and ultrasound imaging, and terahertz for the terahertz imaging. A smaller or larger L can also be used to shift the transparent band from the UV region to even the terahertz region according to the specific application.

**3.5. Understanding of**  $T_{GH}(\lambda, \phi)$ **.** To figure out the reason for the highly improved transmission at P<sub>3</sub><sup>90°</sup> and further understand the spectral features of  $T_{\rm GH}(\lambda, \phi)$ , FDTD calculations are performed based on the representative NGonNH structure (L = 750 nm, D = 563 nm). Figure 7a,b shows the comparison of the experimental (solid curves) and calculated (dashed curves)  $T_{\rm GH}(\lambda, \phi)$  at  $\phi = 90^{\circ}$  and  $0^{\circ}$ , respectively. The spectra were calculated by importing the MATLAB calculated structures into the FDTD software. Overall, the calculated results are in good agreement with the experimental spectra except that the dips in the calculated spectra are sharper and stronger, which is due to the use of periodic boundary conditions in the calculations. For the experimental measurement, since the illuminated area is larger (the diameter of the light spot is  $\sim$ 2 mm), there are many statistical variations of the structures in probed area, and the statistic difference among different units causes the broadening of the peaks and dips.

At  $\phi = 90^{\circ}$ , except for an extra dip at  $\lambda = 1240$  nm, the spectral features of  $D_4^{90^\circ}$ ,  $D_5^{90^\circ}$ , and  $P_3^{90^\circ}$  are all well predicted by FDTD calculations. The extra small dip at  $\lambda = 1240$  nm of the calculated results in Figure 7a may be caused by the sharp edge of the imported structure in the calculation. To better understand the origin of the new EOT mode  $P_3^{90^{\circ}}$ , the  $T_{\rm NG}(\lambda, \phi)$  spectra calculated from the corresponding NG structure are also plotted in Figure 7 (the gray dashed curves). The  $P_3^{90^\circ}$  transmission peak of the NGonNH structure is very close to the dip D<sub>NG</sub> of the NG structure. To further confirm this observation, the spectra of  $T_{\rm GH}(\lambda, 90^{\circ})$ ,  $T_{\rm NG}(\lambda, 90^{\circ})$  of NG, and  $T_{\rm NH}(\lambda)$  of different D are plotted in Figure S20. The  $P_3^{90^{\circ}}$  locations of all the NGonNH structures are very close position to the dip  $D_{NG}$  positions of the corresponding NGs (Figures 7a and S20), indicating that the origin of  $P_3^{90^{\circ}}$  must be related to  $D_{NG}$ . Figure 7c-e plots the local  $E_z$ -field distributions at  $\lambda_{P_2^{90^{\circ}}}$  at the air-grating, grating-hole, and hole-glass interfaces, respectively. The local  $E_z$ -field distribution of D<sub>NG</sub> of the NG structure is also shown in Figure S21 as a reference. The local  $E_z$ -field distribution at  $\lambda_{P_2^{90^{\circ}}}$  shows a strong localized dipole resonant mode of the two triangles inside the hole, and a weak resonance of the NH can also be observed. The local  $E_z$ -field distribution of  $D_{NG}$  in Figure S21 also shows similar results. These results indicate that the appearance of  $P_3^{90^\circ}$  should be attributed to the localized plasmon coupling between the triangles and the NH. This coupling funnels the light into the small gap between the two triangles and reradiates electromagnetic waves through the gap, leading to an enhanced transmission. Difference in  $P_3^{90^\circ}$  and the dips  $D_4^{90^\circ}$  and  $D_5^{90^\circ}$  correspond to higher energy resonances, suggesting that they may be related to higher-order plasmon resonances.  $^{53,54}$  The  $E_z$ -field distribution shown in Figure S22 indicates that the resonance at  $\lambda_{D_4^{90^\circ}}$  and  $\lambda_{D_5^{90^\circ}}$  are the results of the overlapping between the hexapole mode of NGonNH and the surface plasmon polaritons (SPP) mode P2 as well as the interference between the octupolar mode and SPP mode P<sub>2</sub>. <sup>26</sup> At  $\phi = 0^{\circ}$ , both the calculated and experimental spectra exhibit a broad peak with a dip  $D_3^{0^{\circ}}$  ( $\lambda_{D_3^{0^{\circ}}} = 1230$  nm for FDTD and  $\lambda_{\rm D_2^{0^{\circ}}} = 1260 \text{ nm}$  for experiment). The other dip at 1032 nm from the FDTD (D<sub>4</sub>) spectrum is rather weak at  $\phi = 0^{\circ}$  and we did not observe it experimentally. The  $E_z$ -field distribution shown in Figure S22 indicates that the  $D_3^{0^{\circ}}$  is the result of the overlapping between the quadrupole mode of NGonNH and the SPP mode P<sub>2</sub> in the compound hole array.<sup>26</sup> A detailed discussion about the dips is found in Section S12.

To compare the overall polarization dependence  $T_{\rm GH}(\lambda,\phi)$  of different structures, we plot  $T_{\rm P_3}$  versus  $\phi$  in Figure S23 for different D. Overall, the polar plots of  $T_{\rm P_3}$  are dumbbell-shaped curves, and they can be well fitted by

$$T_{P}(\phi) = T_{*}(1 - \alpha^{2}\cos^{2}\phi)$$

(the dashed curves in Figure S23), consistent with several previous studies for the in-plane dipole mode resonance. When D decreases from 612 to 520 nm,  $\alpha$  increases from 0.34 (D = 612 nm) to 0.58 (D = 563 nm), 0.64 (D = 520 nm), and 0.63 (D = 444 nm), which is different from almost invariant  $\alpha$ 

for  $R_{\rm GH}(\phi)$ , indicating a stronger  $\phi$ -dependence optical property for the NGonNH structures.

# 4. CONCLUSIONS

In summary, based on the NSL and OAD, we have designed the NGonNH structures over large substrate areas, and the structures show significantly improved electric property and dual-band optical transparency. The geometries of the formed NGonNH can be precisely varied by controlling the size of the PSNS, the etching duration of the PSNS, the orientation of the PSNS monolayer domain, and the vapor incident angle during OAD. Most of the NGonNH structures have shown reduced resistances when compared to that of NH array. Such a reduced and anisotropic resistance behavior is predicted by a two-dimensional hexagonal resistor network model. In addition, polarization-dependent and highly improved optical transmissions with tunable spectral ranges are also obtained due to the plasmonic coupling effect as well as the anisotropic morphology and can be predicted by FDTD calculations. Dualtransmission regions (visible and NIR) can be switched by a polarization angle, which is very unique and has the potential application of dual-functionality for TMFs. In particular, a NGonNH structure with a low sheet resistance of 4.53  $\Omega$ /sq, a high average transmittance of 75.4% over the 1000 to 2500 nm wavelength region, and a Haacke number of 13.1 is realized, which is higher than or comparable to those reported metal NH arrays and TMFs. The Haacke number under  $\phi$  = 90 $^\circ$ polarized light  $(\phi_{
m H-90^\circ})$  is higher than that under nonpolarized light, i.e.,  $\phi_{\rm H-90^\circ}$  = 20.4 for the above NGonNH structure ( $\phi_{\rm H}$ = 13.1). We would like to point out that in these preliminary experiments, many parameters such as materials, grating shape, and metal thickness have not yet been optimized. Even better performance can be expected by designing more advanced compound geometries, for instance, by increasing the thickness of only one pattern (NH or NG) of the NGonNH, while minimizing the other, or altering the shape of the NH or NG by changing the incident angle  $\theta$  (Figure S24). In addition, such a wide-band optical property can also be used for optical filters, and the polarization property can be used for polarization-modulation based optical components or sensors.

### ASSOCIATED CONTENT

# **Solution** Supporting Information

The Supporting Information is available free of charge at https://pubs.acs.org/doi/10.1021/acsaelm.1c00443.

Figure S1 describes the morphology differences between different deposition strategies, Figure S2 describes the shadow mask for orientation-dependent resistance measurement, Figure S3 describes the optical transmission measurement setup, Figures S4 and S5 describe the general setup of FDTD simulation, Figures S6 and S7 describe the effect of the hole size on the resulted NGonNH structures, Figure S8 describes the influence of  $\varphi$  on structure, Figures S9 and S10 and Table S1 describe the improved electric resistance, Figures S11 and S12 describe the infinite honeycomb resistornetwork model, Figures S13 and S14 and Table S2 describe the influence of structure parameters on optical properties, Figures S15–S17 describe the influence of L on morphological and optical properties of the structure, Figures S18-S20 describe the details about the FDTD

NIR

calculations, and Figure S21 describes the polarization angle-dependent optical properties (PDF)

# AUTHOR INFORMATION

## **Corresponding Authors**

Zhengjun Zhang — Key Laboratory of Advanced Materials (MOE), School of Materials Science and Engineering, Tsinghua University, Beijing 100084, P. R. China; orcid.org/0000-0001-8727-6373; Email: zjzhang@tsinghua.edu.cn

Yiping Zhao — Department of Physics and Astronomy, University of Georgia, Athens, Georgia 30602, United States; orcid.org/0000-0002-3710-4159; Email: zhaoy@uga.edu

## **Authors**

Yanfeng Wang — Key Laboratory of Advanced Materials (MOE), School of Materials Science and Engineering, Tsinghua University, Beijing 100084, P. R. China; Department of Physics and Astronomy, University of Georgia, Athens, Georgia 30602, United States; ⊚ orcid.org/0000-0001-7698-6230

Inyoung Choi – Department of Physics and Astronomy, University of Georgia, Athens, Georgia 30602, United States Kaiyuan Zhang – Key Laboratory of Advanced Materials

(MOE), School of Materials Science and Engineering, Tsinghua University, Beijing 100084, P. R. China

Yanjun Yang — Department of Physics and Astronomy, University of Georgia, Athens, Georgia 30602, United States; orcid.org/0000-0002-1822-7364

Shen Ao – Key Laboratory of Advanced Materials (MOE), School of Materials Science and Engineering, Tsinghua University, Beijing 100084, P. R. China

Xiaotian Xue — Key Laboratory of Advanced Materials (MOE), School of Materials Science and Engineering, Tsinghua University, Beijing 100084, P. R. China

Wangyang Fu – Key Laboratory of Advanced Materials (MOE), School of Materials Science and Engineering, Tsinghua University, Beijing 100084, P. R. China

Complete contact information is available at: https://pubs.acs.org/10.1021/acsaelm.1c00443

### **Author Contributions**

The manuscript was written through contributions of all authors. All authors have given approval to the final version of the manuscript.

#### Notes

The authors declare no competing financial interest.

## ACKNOWLEDGMENTS

Y.W., X.X., S.A., and Z.Z. were financially supported by the Basic Science Centre Project of NSFC under Grant no. 51788104 and the Chinese National Natural Science Foundation (no. 51761145045). Y.Y. and Y.Z. were financially supported by the National Science Foundation under Grant no. ECCS-1808271. The authors also thank Zhenxing Li for helping them with the MATLAB programs.

# ABBREVIATIONS

TMF transparent metallic film

NG nanograting NH nanohole

EOT extraordir	nary optical	l transmission
----------------	--------------	----------------

near-infrared

NSL nanosphere lithography PF perforation fraction

TCO transparent conductive oxide

NGonNH NG on NH

FDTD finite difference time domain

FOM figure of merit

TCF transparent conductive films
PSNS polystyrene nanospheres
RIE reactive ion etching
SPP surface plasmon polaritons
OAD oblique angle deposition.

### REFERENCES

- (1) Ahn, S. H.; Guo, L. J. High-Speed Roll-to-Roll Nanoimprint Lithography on Flexible Plastic Substrates. *Adv. Mater.* **2008**, *20*, 2044–2049.
- (2) Kahraman, M.; Daggumati, P.; Kurtulus, O.; Seker, E.; Wachsmann-Hogiu, S. Fabrication and characterization of flexible and tunable plasmonic nanostructures. *Sci Rep.* **2013**, *3*, No. 3396.
- (3) Qiu, T.; Akinoglu, E. M.; Luo, B.; Giersig, M.; Liang, M.; Ning, J.; Zhi, L. Shape Control of Periodic Metallic Nanostructures for Transparent Conductive Films. *Part. Part. Syst. Charact.* **2017**, 34, No. 1600262.
- (4) Bao, C.; Yang, J.; Gao, H.; Li, F.; Yao, Y.; Yang, B.; Fu, G.; Zhou, X.; Yu, T.; Qin, Y.; Liu, J.; Zou, Z. In Situ Fabrication of Highly Conductive Metal Nanowire Networks with High Transmittance from Deep-Ultraviolet to Near-Infrared. *ACS Nano* **2015**, *9*, 2502–2509.
- (5) Sannicolo, T.; Lagrange, M.; Cabos, A.; Celle, C.; Simonato, J. P.; Bellet, D. Metallic Nanowire-Based Transparent Electrodes for Next Generation Flexible Devices: A Review. *Small* **2016**, *12*, 6052–6075
- (6) Zeng, B.; Gao, Y.; Bartoli, F. J. Ultrathin nanostructured metals for highly transmissive plasmonic subtractive color filters. *Sci Rep.* **2013**, *3*, No. 2840.
- (7) Wang, S.; Dong, H.; Sun, F.; Zhang, W.; Liang, Y.; Tian, L.; Wang, P.; Yin, X.; Li, G. Large-Area Fabrication of Highly Tunable Hybrid Plasmonic—Photonic Structures Based on Colloidal Lithography and a Photoreconfigurable Polymer. *Adv. Opt. Mater.* **2019**, *7*, No. 1900483.
- (8) Morfa, A. J.; Akinoglu, E. M.; Subbiah, J.; Giersig, M.; Mulvaney, P. Transparent Metal Electrodes From Ordered Nanosphere Arrays. *J. Appl. Phys.* **2013**, *114*, No. 054502.
- (9) Oddone, V.; Giersig, M. Nanosphere lithography with variable deposition angle for the production of one-directional transparent conductors. *Phys. Status Solidi RRL* **2017**, *11*, No. 1700005.
- (10) Ho, Y.-H.; Chen, K.-Y.; Liu, S.-W.; Chang, Y.-T.; Huang, D.-W.; Wei, P.-K. Transparent and Conductive Metallic Electrodes Fabricated by Using Nanosphere Lithography. *Org. Electron.* **2011**, *12*, 961–965
- (11) Barnes, T. M.; Reese, M. O.; Bergeson, J. D.; Larsen, B. A.; Blackburn, J. L.; Beard, M. C.; Bult, J.; Van De Lagemaat, J. Comparing the Fundamental Physics and Device Performance of Transparent, Conductive Nanostructured Networks with Conventional Transparent Conducting Oxides. *Adv. Energy Mater.* **2012**, *2*, 353–360.
- (12) Hu, L.; Kim, H. S.; Lee, J.-Y.; Peumans, P.; Cui, Y. Scalable Coating and Properties of Transparent, Flexible, Silver Nanowire Electrodes. *ACS Nano* **2010**, *4*, 2955–2963.
- (13) Ebbesen, T. W.; Lezec, H. J.; Ghaemi, H. F.; Thio, T.; Wolff, P. A. Extraordinary optical transmission through sub-wavelength hole arrays. *Nature* **1998**, *391*, 667–669.
- (14) Melentiev, P. N.; Afanasiev, A. E.; Kuzin, A. A.; Gusev, V. M.; Kompanets, O. N.; Esenaliev, R. O.; Balykin, V. I. Split Hole Resonator: A Nanoscale UV Light Source. *Nano Lett.* **2016**, *16*, 1138–1142.

- (15) Lezec, H. J.; Thio, T. Diffracted evanescent wave model for enhanced and suppressed optical transmission through subwavelength hole arrays. *Opt. Express* **2004**, *12*, 3629–3651.
- (16) Qiu, T.; Luo, B.; Akinoglu, E. M.; Yun, J. H.; Gentle, I. R.; Wang, L. Trilayer Nanomesh Films with Tunable Wettability as Highly Transparent, Flexible, and Recyclable Electrodes. *Adv. Funct. Mater.* **2020**, *30*, No. 2002556.
- (17) Sakudo, A. Near-infrared spectroscopy for medical applications: Current status and future perspectives. *Clin. Chim. Acta* **2016**, 455, 181–188.
- (18) Wang, Q.; Raglione, M.; Li, B.; Jin, X.; Toor, F.; Arnold, M.; Ding, H. High Throughput Laser Process of Transparent Conducting Surfaces for Terahertz Bandpass Ultrathin Metamaterials. *Sci. Rep.* **2019**, *9*, No. 3083.
- (19) Colson, P.; Henrist, C.; Cloots, R. Nanosphere Lithography: A Powerful Method for the Controlled Manufacturing of Nanomaterials. *J. Nanomater.* **2013**, 2013, 1–19.
- (20) Wood, R. W. Anomalous Diffraction Gratings. *Phys. Rev.* 1935, 48, 928–936.
- (21) Rodrigo, S. G. Extraordinary Optical Transmission. In *Optical Properties of Nanostructured Metallic Systems*; Springer-Verlag, Berlin, 2012; pp 37–75.
- (22) Torrisi, G.; Luis, J. S.; Sanchez-Sobrado, O.; Raciti, R.; Mendes, M. J.; Águas, H.; Fortunato, E.; Martins, R.; Terrasi, A. Colloidal-structured metallic micro-grids: High performance transparent electrodes in the red and infrared range. *Sol. Energy Mater. Sol. Cells* **2019**, 197, 7–12.
- (23) Wei, H.; Hakanson, U.; Yang, Z.; Hook, F.; Xu, H. Individual nanometer hole-particle pairs for surface-enhanced Raman scattering. *Small* **2008**, *4*, 1296–1300.
- (24) Wu, S.; Wang, Q.-J.; Yin, X.-G.; Li, J.-Q.; Zhu, D.; Liu, S.-Q.; Zhu, Y.-Y. Enhanced Optical Transmission: Role of the Localized Surface Plasmon. *Appl. Phys. Lett.* **2008**, 93, No. 101113.
- (25) Du, B.; Yang, Y.; Zhang, Y.; Jia, P.; Ebendorff-Heidepriem, H.; Ruan, Y.; Yang, D. Enhancement of extraordinary optical transmission and sensing performance through coupling between metal nanohole and nanoparticle arrays. *J. Phys. D: Appl. Phys.* **2019**, *52*, No. 275201.
- (26) Li, L.; Liang, Y.; Peng, W.; Liu, Y. Fano-like Resonances in the Binary Elliptical Nanoring Resonator Array. *Opt. Mater. Express* **2018**, *8*, 2131–2139.
- (27) Larson, S.; Luong, H.; Song, C.; Zhao, Y. Dipole Radiation-Induced Extraordinary Optical Transmission for Silver Nanorod-Covered Silver Nanohole Arrays. *J. Phys. Chem. C* **2019**, *123*, 5634–5641.
- (28) Wang, Y.; Chong, H. B.; Zhang, Z.; Zhao, Y. Large-Area Fabrication of Complex Nanohole Arrays with Highly Tunable Plasmonic Properties. ACS Appl. Mater. Interfaces 2020, 12, 37435—37443.
- (29) Wang, Y.; Luong, H.; Zhang, Z.; Zhao, Y. Coupling between plasmonic nanohole array and nanorod arrays: The emerging of a new extraordinary optical transmission mode and epsilon-near-zero property. J. Phys. D: Appl. Phys. 2020, 53, No. 275202.
- (30) Li, Z.; Wang, G.; Li, Ż.; Cheng, Z.; Zhou, G.; Li, S. Flexible Transparent Electrodes Based on Gold Nanomeshes. *Nanoscale Res. Lett.* **2019**, *14*, No. 132.
- (31) Skehan, C.; Ai, B.; Larson, S. R.; Stone, K. M.; Dennis, W. M.; Zhao, Y. Plasmonic and SERS performances of compound nanohole arrays fabricated by shadow sphere lithography. *Nanotechnology* **2018**, 29, No. 095301.
- (32) Ai, B.; Song, C.; Bradley, L.; Zhao, Y. Strong Fano Resonance Excited in an Array of Nanoparticle-in-Ring Nanostructures for Dual Plasmonic Sensor Applications. *J. Phys. Chem. C* **2018**, *122*, 20935–20944.
- (33) Ai, B.; Luong, H. M.; Zhao, Y. Chiral nanohole arrays. *Nanoscale* **2020**, *12*, 2479–2491.
- (34) Ingram, W. M.; Han, C.; Zhang, Q.; Zhao, Y. Optimization of Ag-Coated Polystyrene Nanosphere Substrates for Quantitative Surface-Enhanced Raman Spectroscopy Analysis. *J. Phys. Chem. C* **2015**, *119*, 27639–27648.

- (35) Larsen, G. K.; He, Y.; Ingram, W.; Zhao, Y. Hidden Chirality in Superficially Racemic Patchy Silver Films. *Nano Lett.* **2013**, *13*, 6228–6232.
- (36) He, Y.; Larsen, G. K.; Ingram, W.; Zhao, Y. Tunable three-dimensional helically stacked plasmonic layers on nanosphere monolayers. *Nano Lett.* **2014**, *14*, 1976–1981.
- (37) He, Y.; Lawrence, K.; Ingram, W.; Zhao, Y. Strong Local Chiroptical Response in Racemic Patchy Silver Films: Enabling a Large-Area Chiroptical Device. *ACS Photonics* **2015**, *2*, 1246–1252.
- (38) He, Y.; Wang, X.; Ingram, W.; Ai, B.; Zhao, Y. Optimized Fan-Shaped Chiral Metamaterial as an Ultrathin Narrow-Band Circular Polarizer at Visible Frequencies. *Nanotechnology* **2018**, 29, No. 165301.
- (39) Palik, E. D. Handbook of Optical Constants of Solids; Academic Press: Orlando, FL, 1985.
- (40) Yang, M.; Feng, J.; Li, G.; Zhang, Q. Tungsten-doped In2O3 transparent conductive films with high transmittance in near-infrared region. *J. Cryst. Growth* **2008**, *310*, 3474–3477.
- (41) Huo, X.; Jiang, S.; Liu, P.; Shen, M.; Qiu, S.; Li, M.-Y. Molybdenum and tungsten doped SnO2 transparent conductive thin films with broadband high transmittance between the visible and near-infrared regions. *CrystEngComm* **2017**, *19*, 4413–4423.
- (42) Parthiban, S.; Elangovan, E.; Ramamurthi, K.; Martins, R.; Fortunato, E. Investigations on high visible to near infrared transparent and high mobility Mo doped In2O3 thin films prepared by spray pyrolysis technique. *Sol. Energy Mater. Sol. Cells* **2010**, *94*, 406–412.
- (43) Wang, L.; Yang, Y.; Marks, T. J.; Liu, Z.; Ho, S.-T. Near-infrared transparent electrodes for precision Teng—Man electro-optic measurements: In2O3 thin-film electrodes with tunable near-infrared transparency. *Appl. Phys. Lett.* **2005**, *87*, No. 161107.
- (44) Choi, K.-H.; Kim, J.; Noh, Y.-J.; Na, S.-I.; Kim, H.-K. Ag nanowire-embedded ITO films as a near-infrared transparent and flexible anode for flexible organic solar cells. *Sol. Energy Mater. Sol. Cells* **2013**, *110*, 147–153.
- (45) Hu, L.; Hecht, D. S.; Grüner, G. Infrared transparent carbon nanotube thin films. *Appl. Phys. Lett.* **2009**, *94*, No. 081103.
- (46) Kalita, G.; Matsushima, M.; Uchida, H.; Wakita, K.; Umeno, M. Graphene constructed carbon thin films as transparent electrodes for solar cell applications. *J. Mater. Chem.* **2010**, *20*, 9713–9717.
- (47) Liu, H.-D.; Zhao, Y.-P.; Ramanath, G.; Murarka, S. P.; Wang, G.-C. Thickness dependent electrical resistivity of ultrathin (<40 nm) Cu films. *Thin Solid Films* **2001**, 384, 151–156.
- (48) Li, M.; Zhao, Y.-P.; Wang, G.-C. In situ measurement of thickness dependent electrical resistance of ultrathin Co films on SiO2/Si(111) substrate. *J. Vac. Sci. Technol., A* **2000**, *18*, 2992–2996.
- (49) Atkinson, D.; Van Steenwijk, F. J. Infinite resistive lattices. *Am. J. Phys.* **1999**, *67*, 486–492.
- (50) Martin-Moreno, L.; Garcia-Vidal, F. J.; Lezec, H. J.; Pellerin, K. M.; Thio, T.; Pendry, J. B.; Ebbesen, T. W. Theory of Extraordinary Optical Transmission through Subwavelength Hole Arrays. *Phys. Rev. Lett.* **2001**, *86*, 1114–1117.
- (51) Haacke, G. New figure of merit for transparent conductors. *J. Appl. Phys.* **1976**, *47*, 4086–4089.
- (52) Wang, Y.; Xu, M.; Li, J.; Ma, J.; Wang, X.; Wei, Z.; Chu, X.; Fang, X.; Jin, F. Sol-combustion synthesis of Al-doped ZnO transparent conductive film at low temperature. *Surf. Coat. Technol.* **2017**, 330, 255–259.
- (53) Liu, H.; Wu, X.; Li, B.; Xu, C.; Zhang, G.; Zheng, L. Fano resonance in two-intersecting nanorings: Multiple layers of plasmon hybridizations. *Appl. Phys. Lett.* **2012**, *100*, No. 153114.
- (54) Hao, F.; Sonnefraud, Y.; Dorpe, P. V.; Maier, S. A.; Halas, N. J.; Nordlander, P. Symmetry Breaking in Plasmonic Nanocavities: Subradiant LSPR Sensing and a Tunable Fano Resonance. *Nano Lett.* **2008**, *8*, 3983–3988.
- (55) Cooper, C. T.; Rodriguez, M.; Blair, S.; Shumaker-Parry, J. S. Polarization Anisotropy of Multiple Localized Plasmon Resonance Modes in Noble Metal Nanocrescents. *J. Phys. Chem. C* **2014**, *118*, 1167–1173.

- (56) Huang, Y.; Kim, D. H. Dark-Field Microscopy Studies of Polarization-Dependent Plasmonic Resonance of Single Gold Nanorods: Rainbow Nanoparticles. *Nanoscale* **2011**, *3*, 3228–3232.
- (57) Itoh, T.; Biju, V.; Ishikawa, M.; Kikkawa, Y.; Hashimoto, K.; Ikehata, A.; Ozaki, Y. Surface-Enhanced Resonance Raman Scattering and Background Light Emission Coupled with Plasmon of Single Ag Nanoaggregates. *J. Chem. Phys.* **2006**, *124*, No. 134708.
- (58) Wei, H.; Hao, F.; Huang, Y.; Wang, W.; Nordlander, P.; Xu, H. Polarization Dependence of Surface-Enhanced Raman Scattering in Gold Nanoparticle-Nanowire Systems. *Nano Lett.* **2008**, *8*, 2497–2502.
- (59) Ming, T.; Zhao, L.; Yang, Z.; Chen, H.; Sun, L.; Wang, J.; Yan, C. Strong Polarization Dependence of Plasmon-Enhanced Fluorescence on Single Gold Nanorods. *Nano Lett.* **2009**, *9*, 3806–3903.
- (60) Palasantzas, G.; Zhao, Y. P.; Wang, G. C.; Lu, T. M.; Barnas, J.; De Hosson, J. T. M. Electrical conductivity and thin-film growth dynamics. *Phys. Rev. B* **2000**, *61*, 11109–11117.